Available online at www.sciencedirect.com
SCIENCE DIRECT®
Journal of Nuclear Materials 336 (2005) 251–260
journal of nuclear materials
www.elsevier.com/locate/jnucmat

Radiation effects in ferrate garnet

S. Utsunomiya [a], S. Yudintsev [b], R.C. Ewing [a,*]

[a] Department of Geological Sciences, University of Michigan, 425 East University Ave., Ann Arbor, MI 48109-1063, USA
[b] Institute of Geology of Ore Deposits, Russian Academy of Sciences, Staromonetny 35, 109017 Moscow, Russia

Received 7 July 2004; accepted 14 September 2004

Abstract

Radiation effects in four synthetic ferrate garnets ($A_3B_2(XO_4)_3$, *Ia3d*, $Z = 8$) were examined by ion beam irradiations with in situ observation ($T = 298$–873 K) using transmission electron microscopy (TEM) at the IVEM Tandem Facility at Argonne National Laboratory. The garnet compositions include: A = Ca, Gd, Th, and Ce; B = Zr, Fe. The critical amorphization temperatures (T_c), the temperature above which the target material cannot be amorphized due to dynamic annealing, were between 820 and 870 K. The amorphization doses at room temperature are between 0.17 and 0.19 dpa (displacement per atom), which is similar to that of silicate- and aluminate-garnets. The small variations in the amorphization dose and T_c of the different compositions suggest that radiation effects in ferrate garnets are structurally constrained. Qualitative analyses of the valence states of Ce and Fe in garnet before and after irradiation were completed using electron energy-loss spectroscopy (EELS). The Ce and Fe in the unirradiated garnet were dominantly trivalent and divalent, respectively. The characteristic peaks of Ce^{4+}, at ~5 eV higher energy for the M-edges, were present in unirradiated garnet as a minor peak, and the peaks did not disappear after complete amorphization, suggesting that the valence state did not change significantly. EELS analysis was conducted on a nearly pure andradite, $Ca_3Fe_2Si_3O_{12}$, which ideally contains only ferric iron. The andradite was amorphized at 0.18 dpa. EELS analysis revealed that some of ferric iron was converted to ferrous iron during the irradiation.

1. Introduction

Radiation effects in ceramics have been extensively investigated as part of the effort to develop nuclear waste forms for the immobilization of actinides, particularly plutonium (e.g. [1–4]). Many minerals have been proposed as potential actinide waste forms, and recently garnet structures have been synthesized that incorporate actinides [5–7]. Ca-bearing garnets have been of interest because variations in the Ca/Sr composition can be used to maintain charge balance [5].

Radiation effects in some of the synthetic and natural garnets have been examined by heavy-ion irradiations and in situ transmission electron microscopy (TEM) [8,9]. Most of the garnets were amorphized at doses of 0.2 dpa (displacement per atom) at room temperature, and their critical amorphization temperatures (T_c), the temperature above which the material does not amorphize due to annealing, were in the range of 800–1100 K. However, all of these synthetic, garnet-host ceramics contained large amounts of other phases such

* Corresponding author. Tel.: +1 734 736 9295; fax: +1 734 647 5706.
E-mail address: rodewing@umich.edu (R.C. Ewing).

0022-3115/$ - see front matter © 2004 Elsevier B.V. All rights reserved.
doi:10.1016/j.jnucmat.2004.09.020

as britholite, $Ca_2RE_8(SiO_4)_6O_2$, and calcium uranate, $CaUO_4$. Although the uranate was extremely durable to ion irradiation in the range of the amorphization dose of garnets, radiation effects in britholite, which coexisted in garnet-host ceramics, were apparent during the ion irradiations [10]. The amorphization dose at room temperature and T_c of the britholite were close to the values of the garnets [10].

Garnet, A_3B_2 $(XO_4)_3$ ($Ia3d$; $Z = 8$), can include various cations in the X-site, as well as the A- and B-sites. The X-site is usually occupied by Si in natural garnet, but the other cations, such as Al, Fe, and Ga, can also occupy the X-site. Both the A- and B-sites can incorporate other impurities such as rare earth elements and actinides. Fig. 1(a) shows the structure of andradite, $Ca_3Fe_2Si_3O_{12}$, along the [1 0 0]. The arrows indicate vacant sites in the structure, which correspond to the white dots in a simulated image of high-resolution TEM at Schertzer focus (Fig. 1(b)).

In the present study, ion irradiation experiments were completed on the synthetic garnets produced by a joint program of US DOE Office of Basic Energy Sciences and the Russian Academy of Sciences. The purpose of the present study is to evaluate the susceptibility of these synthetic garnet compositions to amorphization. Radiation-induced phases transformations, such as nanocrystallization and/or decomposition, have been extensively studied mainly for applications in materials science. From the point of view of nuclear waste form development, the redox state of the material after irradiation is important because the redox state of actinides significantly influences their mobility. However, few studies have focused on the radiation-induced changes in valence state of elements in high-level nuclear waste forms. Thus, the second purpose of this study was to analyze the valence states of the redox-coupled elements in unirradiated and fully-amorphized garnets under well-controlled ion irradiation experiments.

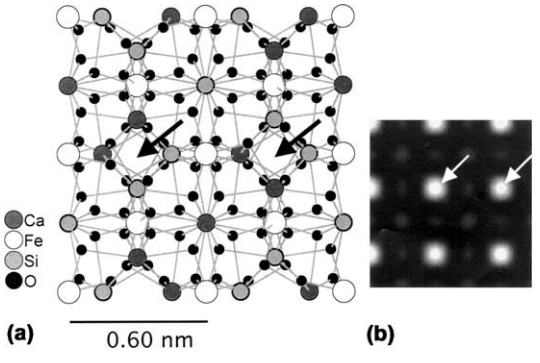

Fig. 1. (a) Structure of andradite, $Ca_3Fe_2Si_3O_{12}$, a typical garnet viewed along [0 0 1]. (b) Computer simulated HRTEM image of andradite at the Schertzer focus along the same zone axis. Bright spots in the image correspond to the vacant sites in the structure (indicated by the arrows), which will be characteristic of the experimentally obtained HRTEM images.

2. Experimental methods

The chemical composition of the garnets was determined by electron microprobe analysis, EMPA (Cameca, SX-100). The samples were analyzed by a focused beam spot (~5 μm) with 20 nA and 20 keV. Counting times are 30 s for all elements. The standard specimens used for the calibration were; andradite, $Ca_3Fe_2Si_3O_{12}$, for Ca (K_α) and Fe (K_α); zircon, $ZrSiO_4$, for Zr (L_α); $CePO_4$ for Ce (L_α); $GdPO_4$ for Gd (M_α); and thorite, $ThSiO_4$, for Th (M_α). The Cameca PAP correction routine (modified ZAF) was used for data reduction. Interferences by overlapping peaks were checked before setting up the data acquisition condition.

Back-scattered electron (BSE) images were observed with semi-quantitative analyses by field-emission gun scanning electron microscopy (FE-SEM, Philips XL30). Thin foil specimens for TEM (transmission electron microscopy) were prepared by mechanical polishing to a thickness of a few tens of micrometer, followed by ion milling using 4.0 keV Ar^+. Before ion irradiations, all TEM specimens were observed using an optical microscope, and images of all specimens were made to confirm the location of the minor perovskite coexisting with the garnet. Garnets and the other minor phases in the starting materials were characterized in detail using high-resolution TEM (HRTEM) and high-angle annular dark-field scanning transmission electron microscopy (HAADF-STEM) using a JEOL 2010F. Contrast in the HAADF-STEM image is correlated to the atomic mass and the thickness of the specimen [11].

The thin foil specimens on TEM grids were irradiated with in situ TEM observation using 1.0 MeV Kr^{2+} in the IVEM (intermediate-voltage electron microscope) at the Tandem Facility of Argonne National Laboratory. The system and operation of the facility is the same as in previous ion irradiation experiments (e.g. [12]). Ion flux of the irradiation was varied over a small range between 1.9 and 3.1×10^{15} ions/m^2/s. The temperature of TEM specimens during irradiation was adjusted to be constant in the range from room temperature to 873 K. Selected-area electron diffraction (SAED) patterns were used to monitor the amorphization process during intervals of increasing ion fluence. Subsequent observations of the irradiated specimens were completed by HRTEM and HAADF-STEM. High-resolution HAADF-STEM was conducted using 0.2 nm of the STEM probe, and the inner angle of HAADF detector was 110 mrad.

The critical amorphization fluence, F_c, (ions/cm^2) was converted to the critical amorphization dose in units of displacement per atom (dpa) and also to the kinetic energy transferred to each target atom through nuclear

collision (E_n) using SRIM 2003 (the stopping and range of ions in matter) [13]. Equations for the conversion followed the procedure described in previous studies [10,14,15]. The required parameters for the conversion were obtained as the average value at ~150 nm of depth. The displacement energy (E_d) of Zr and O used in the calculation were 79 and 47 eV, respectively [16]. The E_d for the other cations was assumed to be 25 eV.

The oxidation states of Ce and Fe were qualitatively analyzed using parallel electron energy-loss spectroscopy (PEELS) with a Gatan Imaging Filter system. An advantage of EELS analysis is that in situ analysis of nanometer-sized areas can be made during TEM observation [17]. The JEOL2010F used in this study has the FWHM (full-width at half maxima) of the zero loss peak in EELS of ~0.9 eV for the 4.0 s acquisition time at the best energy resolution. The FWHM becomes larger than 1.0 eV when using the TEM mode for a longer acquisition time, which means a loss of energy resolution. Because the energy resolution was not high enough to do quantitative analysis, the valence state analysis using EELS in this study is qualitative. The spectra were acquired with convergence and collection angles of 12 and 13 mrad, respectively. The entrance aperture of EELS was 0.6 mm, and an energy dispersion of 0.1 eV/channel was used. The thin areas in the specimen were analyzed to minimize the effect of the multiple inelastic scattering on the fine structure of the spectrum profile.

3. Sample description

The garnet samples were produced by cold pressing (200 MPa) followed by sintering in air at 1600 K for 5 h. The procedure for the synthesis of the garnets has been previously described by Yudintsev et al. [7].

The chemical compositions of the garnet are given in Table 1. Based on a consideration of atomic size, Fe is assigned to the X-site and Zr is assigned to the B-site. Excess Fe may be assigned to the B-site. Large cations such as rare earth elements (REE), Ce and Gd, and Th, are incorporated into A-site. Samples 3T- and 45C-garnet contain Gd in the A-site with extra Fe in B-site; whereas, Gd is not present in samples 4T- and 21C-garnet, with only Zr in the B-site.

Fig. 2 shows an optical micrograph and back-scattered electron (BSE) images for the samples. Because there is a small difference in BSE image contrast among phases in 45C, the optical micrograph is also given for 45C. As shown in Fig. 2, both 45C and 21C contain

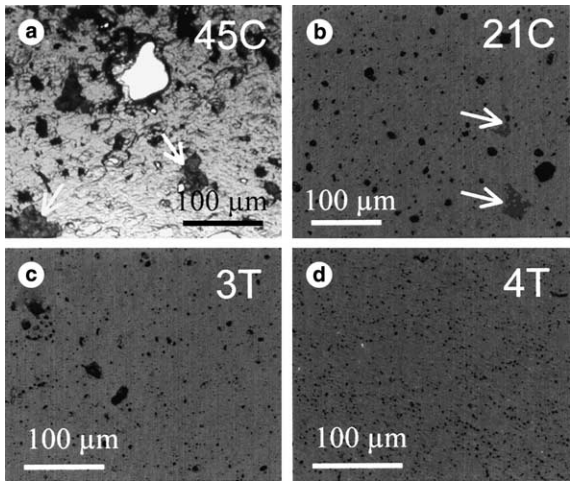

Fig. 2. (a) An optical micrograph and (b–d) BSE images of the garnet samples. Scale bars are 100 μm. The 45C-garnet did not show distinguishable contrast in BSE. Thus, the optical micrograph is shown instead of the BSE image. The small black dots in BSE images are pores. (a) 45C and (b) 21C contain minor amounts of perovskite as indicated by the arrows.

Table 1
Chemical composition (wt%) of the phases in the synthesized garnet-dominant samples analyzed by EMPA

	CaO	FeO[a]	ZrO_2	Ce_2O_3	Gd_2O_3	ThO_2	Total
3T-garnet (n = 6)	9.77 (0.17)	34.0 (1.5)	15.8 (0.51)		21.5 (1.4)	17.1 (0.48)	98.2
45C-garnet (n = 4)	10.4 (0.15)	33.9 (0.15)	18.5 (0.39)	10.7 (0.25)	23.3 (0.58)		96.8
4T-garnet (n = 5)	17.9 (0.06)	28.7 (0.07)	33.7 (0.28)			20.0 (0.27)	100.3
21C-garnet (n = 5)	18.8 (0.30)	30.4 (1.0)	35.7 (1.5)	13.8 (0.35)			98.7

Values in parentheses are the standard deviation. The chemical formula and coordination formula normalized to 12 oxygen are listed as follows:

- 3T garnet: $(Ca_{1.44}Gd_{0.98}Th_{0.53})^{VIII}(Zr_{1.06}Fe_{0.94})^{VI}(Fe_{2.98})^{IV}O_{12}$;
- 45C garnet: $(Ca_{1.50}Gd_{1.03}Ce_{0.53})^{VIII}(Zr_{1.21}Fe_{0.79})^{VI}(Fe_{3.03})^{IV}O_{12}$;
- 4T garnet: $(Ca_{2.37}Th_{0.56})^{VIII}(Zr_{2.03})^{VI}(Fe_{2.96})^{IV}O_{12}$;
- 21C garnet: $(Ca_{2.40}Ce_{0.60})^{VIII}(Zr_{2.08})^{VI}(Fe_{3.03})^{IV}O_{12}$.

The Roman numeral superscripts indicate the coordination number of the indicated cation site.

[a] All Fe are given as FeO.

some impurities, usually perovskite, as indicated by the white arrows. Samples 3T and 4T are relatively homogeneous garnet. Further detailed characterization of the garnet-host materials using HAADF-STEM revealed

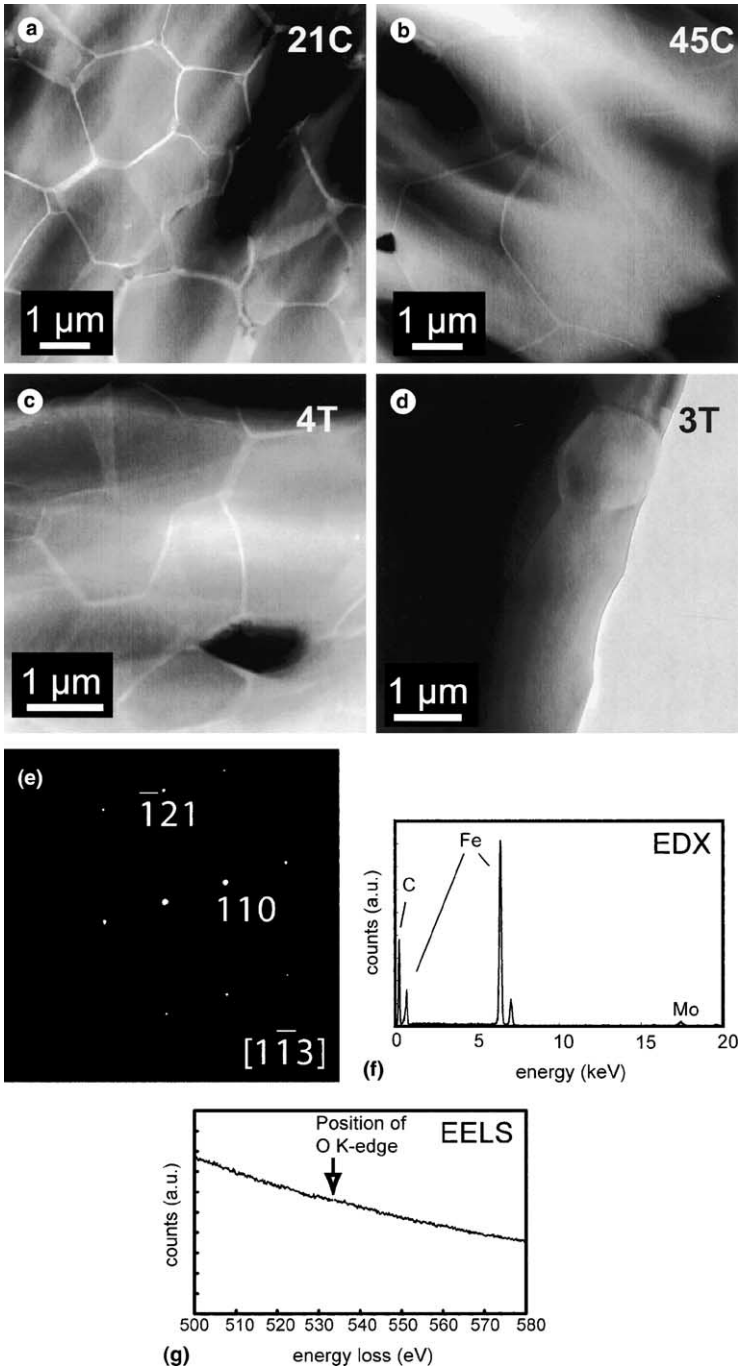

Fig. 3. (a)–(c) HAADF-STEM images of the garnet samples. None of the samples were single crystals, but rather aggregates of small grains of garnets (1–5 μm). (d) The grains are divided by Fe-rich grain boundaries revealing the euhedral shape of the garnet crystals in all samples except 3T. Bright-field TEM image shows a segregation of garnet grains without an Fe-rich grain boundary in 3T. (e) SAED of a Fe-rich phase in the grain boundary, identified as Fe-metal. (f) EDX shows that Fe is the only major element. Molybdenum peak is derived from the TEM specimen grid. (g) EELS confirms the absence of oxygen (~532 eV) in the Fe-rich grain boundary.

that all of the samples consisted of aggregates of garnet at the micron scale, not as a single large crystal (Fig. 3(a)–(d)). The size of the garnet crystals was uniform and approximately 1–5 μm in all of the samples. The grain boundaries of the garnets were filled with Fe-rich phases and appeared to form a honeycomb texture, except for the 3T-garnet. However the HAADF-STEM images can only reveal two dimensional information about the sample because the TEM specimen is prepared as a thin foil. Thus, the actual texture of the grain boundary must form a three dimensional network. In fact, the 21C-garnet revealed a variation in the width of Fe-rich grain boundary indicating that the plane of Fe-rich grain boundary was tilted from the axis of view. The Fe-rich phase in the grain boundary was characterized in detail. The diffraction pattern is consistent with bcc, Fe-metal (Fig. 3(e)), which is supported by the chemical composition consisting of only Fe (Fig. 3(f)) without an oxygen peak at ~532 eV in the EELS profile (Fig. 3(g)). The presence of metallic Fe^0 confirms that these garnets were synthesized under extremely reducing conditions. Another minor phase found in the sample due to their extremely bright contrast under HAADF-STEM was ThO_2 as inclusions at the submicron scale.

4. Results and discussion

4.1. Amorphization of the garnets by ion irradiation

The amorphization fluence, dose, and other parameters were calculated using SRIM 2003 (Table 2). The critical amorphization doses for all of the garnet compositions at room temperature were within a narrow range: 0.17–0.19 dpa, and similar to the amorphization doses of silicate- and aluminate-garnets (~0.20 dpa) [8,9]. The amorphization doses increase greatly at higher temperatures >700 K (Fig. 4). The critical amorphization temperatures, T_c, of the garnets were estimated to be approximately in the range from 820 to 870 K. The range of the variation in T_c values, 50 K, was too small to determine a relative order for the different garnet composition as a function of T_c. Generally, the ratio of electronic to nuclear stopping power (ENSP) can be used to interpret the variation in T_c, and a higher ENSP results in a lower T_c because of the annealing caused by the ionizing radiation [18]. In these samples, ENSPs were 0.94 in 21C, 0.91 in 45C, 0.91 in 3T and 0.92 in 4T. The ENSPs are essentially the same, within a range of 0.03. The narrow range of ENSP values is consistent with the narrow range of T_c values.

Table 2
Summary of amorphization doses and the other parameters of garnets calculated using SRIM 2003; the temperature, T (K); the critical amorphization ion fluence, F_c ($\times 10^{18}$ ions/m^2); collision events, $N_{collision}$ (number/ion/Å); ion energy loss to recoil atoms, E_r (eV/ion/Å); recoil ionization energy loss, I_r (eV/Å); incident ion energy loss to phonon, P_i (eV/Å); displacement per atom, dpa; energy loss through nuclear collision, E_n (eV/atom)

	T (K)	F_c	dpa	E_n
21C	298	1.38	0.17	15.8
$N_{collision}$ = 0.65	573	1.63	0.21	18.7
E_r = 101	673	2.56	0.33	29.5
I_r = 43	773	4.69	0.60	54.0
P_i = 1	873[a]	13.8[a]	1.75[a]	158[a]
45C	298	1.19	0.17	15.3
$N_{collision}$ = 0.74	673	2.31	0.31	27.4
E_r = 108	723	2.31	0.33	29.8
I_r = 43	773	5.63	0.81	72.5
P_i = 1	823[a]	11.9[a]	1.72[a]	153[a]
3T	298	1.25	0.19	15.5
$N_{collision}$ = 0.77	673	1.69	0.26	21.0
E_r = 105	773	2.81	0.43	34.9
I_r = 43	823	5.00	0.76	62.1
P_i = 1				
4T	298	1.38	0.17	16.5
$N_{collision}$ = 0.63	673	1.81	0.23	21.7
E_r = 100	773	2.25	0.28	27.0
I_r = 41	823	5.00	0.63	60.0
P_i = 1				

[a] The target garnets at these temperatures did not become amorphous even at doses 10 times greater than those at the room temperature.

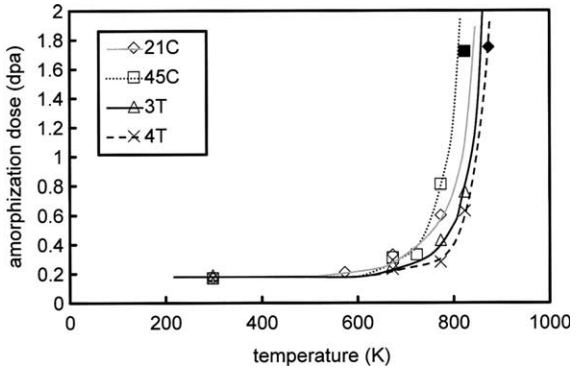

Fig. 4. The amorphization doses (dpa) plotted against temperature (K). The two closed symbols for 21C and 45C at high temperatures indicate that the garnets did not become amorphous, even at the indicated accumulation dose, which is more than 10 times greater than the amorphization dose at the room temperature.

The crystalline-to-aperiodic transition is evident in the SAEDs (selected-area electron diffraction patterns) for the 4T-garnet at the room temperature (Fig. 5). The diffuse halo in the diffraction pattern developed with increasing ion dose, and the intensity of diffraction maxima gradually decreased with increasing dose. The HRTEM images of the radiation-induced transition in the 4T-garnet at the room temperature (viewed along [0 0 1] are shown in Fig. 6. Amorphous domains created by overlapping cascades (indicated by the arrow) are present in crystalline matrix at 0.06 dpa (Fig. 6(b)). The amorphous domains become dominant and nanoscale remnants of crystalline garnet remain in the amorphous matrix at 0.12 dpa (Fig. 6(c)). The orientation of nanosized crystalline remnants is the same; thus, the diffraction maxima do not show streaking (Figs. 5(c) and 6(c)). There are no crystalline domains at 0.17 dpa (Fig. 6(d)). This process of amorphization as evidenced by SAED and HRTEM is consistent with the observations of silicate- and aluminate-garnets [8,9].

HAADF-STEM images of 4T-garnet irradiated at the room temperature showed that the honeycomb texture of the Fe-boundary remained during the ion irradiation (Fig. 7(a)) even after the garnet was fully amorphized, 0.17 dpa (Fig. 7(b)). The Fe-boundary also remained crystalline after 0.17 dpa, as confirmed by HRTEM. This evidence suggests that the Fe metal present at the grain boundary is more durable than the host garnet against radiation damage. However, this Fe-metal portion is chemically unstable under the ambient oxidizing conditions at the Earth's surface. Thus, the grain boundary will be easily dissolved and transformed to Fe-oxides during alteration under oxidizing conditions.

The 4T-garnet irradiated at the room temperature is shown in Fig. 8(a) after a dose of 0.12 dpa. The HRTEM image showed the nanosized crystalline remnants. In a HAADF-STEM image, the nanocrystals in the amorphous matrix appeared as relatively brighter contrast domains, as compared with the surrounding amorphous matrix (Fig. 8(b)). The nanocrystals were confirmed by the lattice images in high-resolution HAADF-STEM (Fig. 8(c)). The advantage of using the HAADF-STEM image is that the image contrast is directly correlated to relative atomic mass in the material, and the contrast in high-resolution (HR-)HAADF-STEM does not change significantly with focus at 'just focus' conditions because the HR-HAADF-STEM image is created through an incoherent imaging process [19,20]. Because high resolution HAADF-STEM imaging is more sensitive to focusing than HRTEM imaging due to a converged beam in STEM mode, the other matrix area was carefully checked by adjusting the focus in order to determine whether the remaining domains were crystalline. The darker matrix area did not reveal any crystalline remnants. There are some conditions under which the amorphous matrix will show darker contrast in HAADF-STEM as a function of variations in thickness, density, periodicity of atoms, and Z-contrast [21]. The first three criteria are physical properties of the specimen, and the Z-contrast is a result of chemical composition. In the present case, the chemical composition of the amorphous domains should not be significantly different from that of the crystalline remnants. Thickness and density in the amorphous domains may have changed from that of the original garnet. As an example, previous studies on radiation effects in zircon have reported

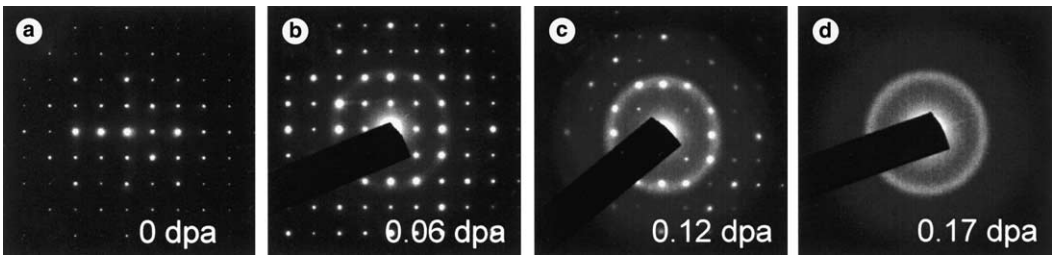

Fig. 5. The SAED patterns of 4T garnet during the irradiation at the room temperature; from (a) 0 dpa to (d) 0.17 dpa.

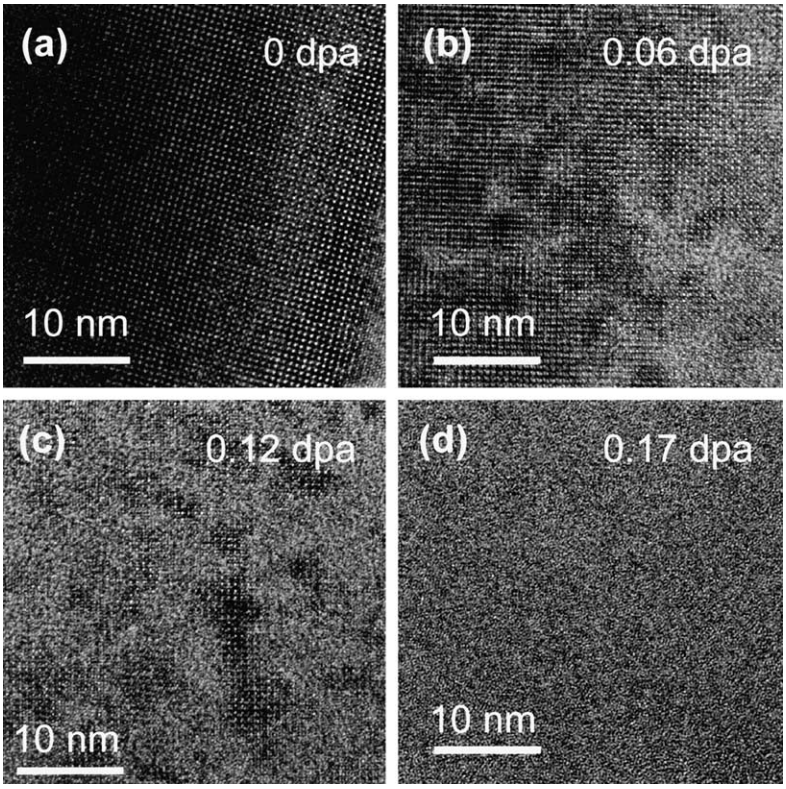

Fig. 6. The HRTEM images of 4T garnet during irradiation at the room temperature; from (a) 0 dpa to (d) 0.17 dpa. The HRTEM images show an array of bright dots which correspond to the white dots in the simulated HRTEM image (Fig. 1(b)).

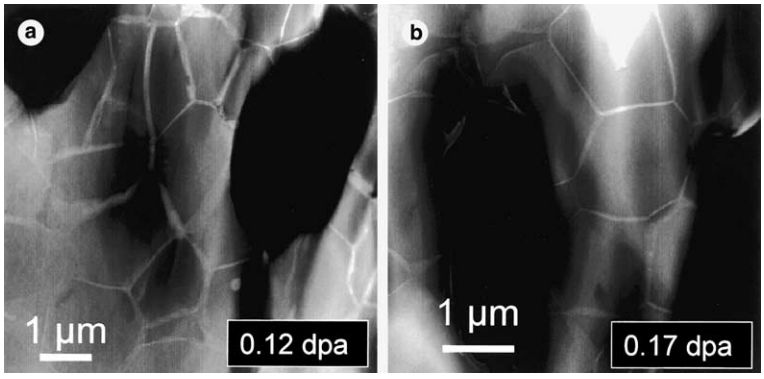

Fig. 7. HAADF-STEM image in 4T showing the presence of Fe-rich grain boundaries during the irradiation at the room temperature: (a) 0.06 dpa and (b) 0.12 dpa.

significant swelling (up to 16% in volume) and density decrease (up to 16%) at saturation doses [22,23]. Swelling may result in an increase in the thickness of the amorphous volume; thus, the thicker amorphous domain is expected to appear as brighter contrast. However, the decrease of density in the amorphous domains played a role in making the contrast darker in the amorphous domains. A loss of periodicity of atomic arrays in the amorphous domain can also give the image of the area a darker contrast. A previous study has also reported that amorphous tracks caused by fission fragments in zircon revealed a darker contrast than the surrounding crystalline area [24]. Thus, the sum of the effects derived from the loss of periodicity and the

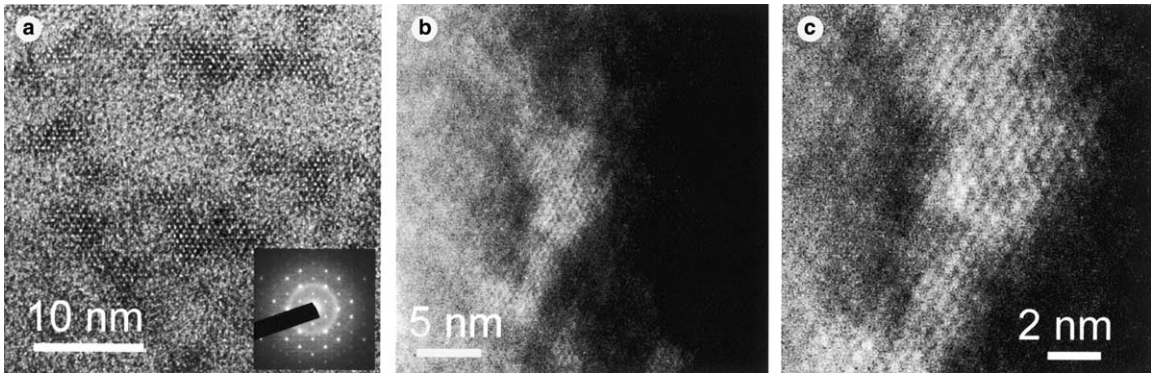

Fig. 8. (a) HRTEM image of 4T at a dose of 0.12 dpa at the room temperature viewed along [1 1 1]. (b) HAADF-STEM image of the same area along [1 1 1] showing the heterogeneous distribution of the bright contrast domain. (c) The high-resolution HAADF-STEM image of the bright area in (b) shows the *Z*-contrast structural information.

decrease in the density of the amorphous domains contributes to the contrast in HAADF-STEM images more than the effect of an increase in the thickness.

4.2. Valence states of Ce and Fe during ion irradiation

The garnet specimens, unirradiated and after the complete amorphization, were analyzed using EELS (electron energy-loss spectroscopy). Polyvalent elements, Ce and Fe, in the garnets were analyzed. Normally, Ce is present as a tri- or tetra-valent cation and Fe is di- or trivalent. Determinations of the valence states of Ce and Fe were systematically conducted in previous studies using the Ce $M_{4,5}$-edge [25] and Fe $L_{2,3}$-edge [26–28] in EELS, respectively. EELS data collected from minerals containing each valence state for both Ce and Fe are given in Fig. 9. The Ce^{3+} $M_{4,5}$-edge of $CePO_4$ showed maximum peak at ~882 and ~900 eV, while the Ce^{4+} $M_{4,5}$-edge of CeO_2 had maximum beaks at ~884 eV and ~901.5 eV associated with characteristic small peaks at ~889 eV and ~906.5 eV. Also, the Fe^{2+} L_3-edge of fayalite showed a maximum peak at ~708 eV with a shoulder peak at a slight higher energy and a weak peak of the L_2-edge at ~720 eV, while Fe^{3+} L_3-edge of andradite showed a maximum peak at ~709.5 eV with a shoulder peak at the slightly lower energy and the L_2-edge appeared as weak broadened peak which ideally has two distinguishable weak peaks. More detailed energies for the peaks and the energies for the minor peaks have been reported in previous studies [25–28], in which the EELS of Ce and Fe in the other minerals also showed almost the same fine structure of EELS for an element of the same valence [25–28]. Thus, the difference in fine structure of EELS for the same valence state in different minerals is small enough for the qualitative analysis of valence state in the present study. Fig. 10(a) and (b) show the EELS of Ce $M_{4,5}$-edge collected from 45C- and 21C-garnets. Each figure includes EELS for unirradiated (0 dpa) and fully-amorphized garnets (D_c). The fine structure and the energy loss of Ce $M_{4,5}$-edge in both unirradiated 45C- and 21C-garnets are similar to those of Ce^{3+} in $CePO_4$, indicating that Ce^{3+} is dominant in these unirradiated garnets. EELS of Ce $M_{4,5}$-edge of fully amorphized 45C- and 21C-garnets did not reveal significant changes in the fine structure of

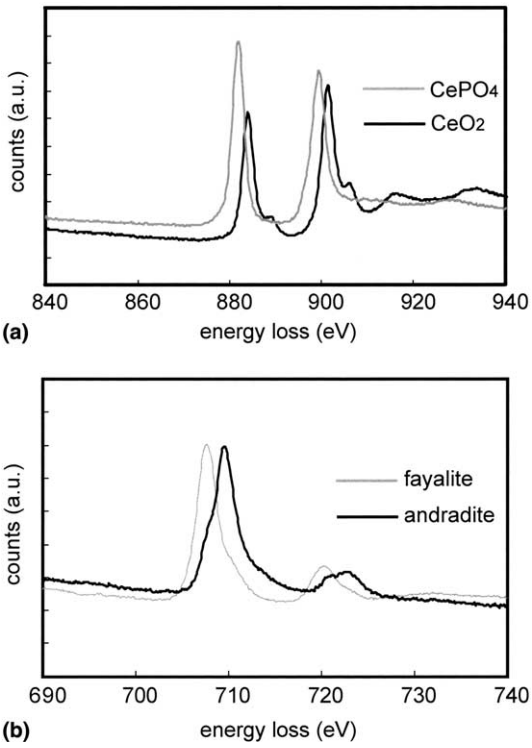

Fig. 9. (a) Ce $M_{4,5}$-edges of Ce^{3+}- and Ce^{4+}-bearing minerals; $CePO_4$ and CeO_2, respectively. (b) Fe $L_{2,3}$-edges of Fe^{2+}- and Fe^{3+}-minerals; fayalite, Fe_2SiO_4, and andradite, respectively.

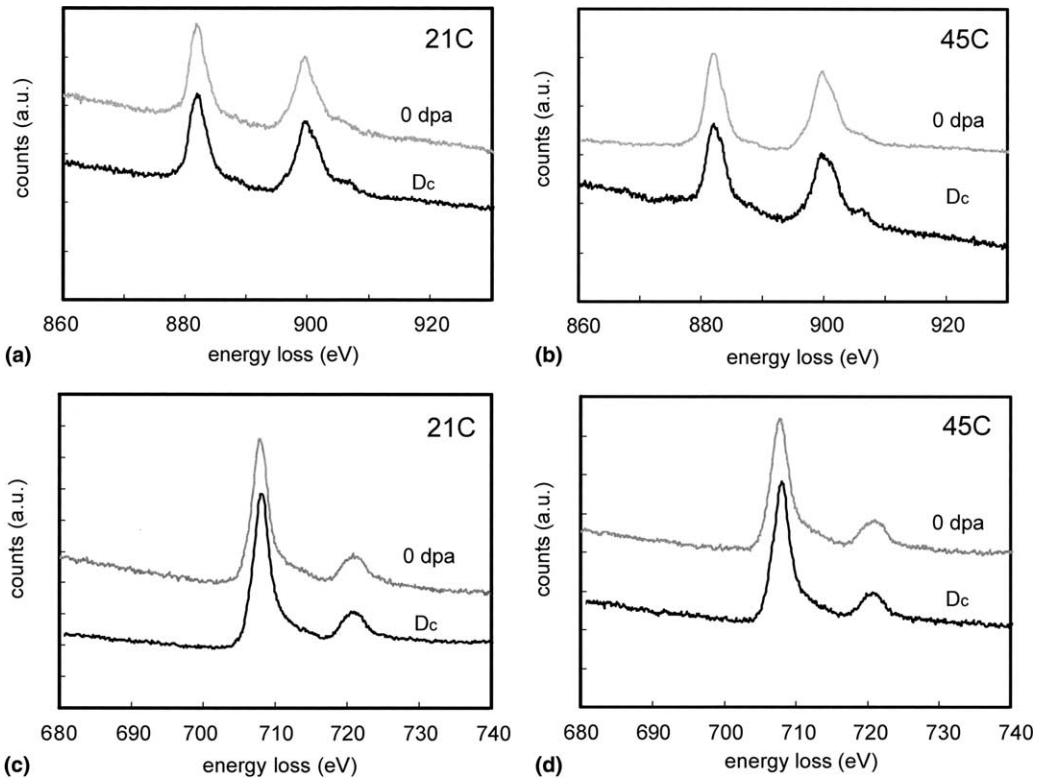

Fig. 10. (a) Ce $M_{4,5}$-edges of unirradiated and fully-amorphized 21C-garnet. (b) Ce $M_{4,5}$-edges of unirradiated and fully-amorphized 45C-garnet. (c) Fe $L_{2,3}$-edges of unirradiated and fully-amorphized 21C-garnet. (d) Fe $L_{2,3}$-edges of unirradiated and fully-amorphized 45C-garnet.

the energy-loss spectra. These spectra suggest that the garnets initially contained Ce^{3+} and the valence of Ce did not change after irradiation at the fully amorphized dose (~0.17 dpa). The small peaks at ~889 and ~906.5 eV which are characteristic in EELS of Ce^{4+} are observed in both 45C and 21C garnets, indicating the presence of a small amount of Ce^{4+} in these unirradiated garnets. These small peaks still remained with the same size after complete amorphization. The Fe $L_{2,3}$-edge of the unirradiated garnets of both compositions, 45C and 21C, revealed similar energy-loss peak position and the fine structure to those of Fe^{2+} in fayalite, indicating that the Fe^{2+} is dominant in these unirradiated garnets. The Fe $L_{2,3}$-edge after the complete amorphization also indicated the presence of Fe^{2+} as the dominant valence state of Fe. Ferric iron may be present at trace concentrations, but it was difficult to separate the small-sized peaks with the energy resolution of the present experiments. The predominance of the reduced form of Ce and Fe in the garnets was expected because of the presence of Fe-metal in the grain boundaries. Summarizing the results of the valence states of Ce and Fe in the garnets, the ion beam irradiation did not oxidize the Ce and Fe in the garnet at the doses required for complete amorphization.

In order to investigate further the reducing effects on the valence state of Fe, an end-member garnet, andradite; $Ca_3Fe_2Si_3O_{12}$, containing almost all Fe^{3+} was also analyzed using EELS. The andradite was amorphized by 0.18 dpa of ion irradiation at room temperature [8]. The EELS of unirradiated andradite was the same as that shown in Fig. 9(b). The Fe $L_{2,3}$-edge in fully-amorphized andradite revealed some variations in the EELS profile. Some areas showed almost the same fine structure and energy-loss peak position to those of Fe^{3+} (Fig. 11(a) and (b)), while the EELS profile in the other area appeared to contain some of Fe^{2+} (Fig. 11(c)). These results suggest that radiation-induced amorphization can cause a slight reduction of the valence state of Fe^{3+} in garnet. The observed variation in valence of Fe may be attributed to the heterogeneity caused by overlapping cascades.

Zang et al. [29] systematically investigated radiation-induced changes in valence state of U in zircon using near-infrared spectroscopy. They found that the ratio of U^{4+}/U^{5+} increased as the radiation dose increased,

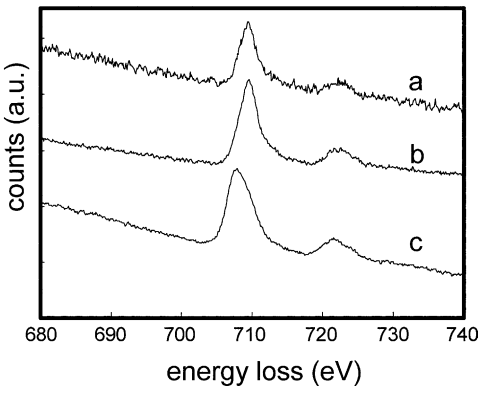

Fig. 11. (a) and (b) Fe $L_{2,3}$-edges of the fully-amorphized andradite show fine structure and the energy-loss peak position of EELS similar to that of unirradiated andradite at some analytical points; (c) the other points indicate the presence of small amount of Fe^{2+}.

confirming that the reducing effects of radiation damage [29]. The reduction in valence state is most likely caused by ionization effects during ion bombardment. In fact, a calculation using SRIM2003 revealed that the total energy dissipated by the ionization in the present experiment was approximately 92–98 eV/Å, which is close to the energy loss through nuclear collisions, 100–108 eV/Å. Thus, there can be ionization effects during irradiation and the effect may cause the reduction of the valence state of the target or recoil atoms, although the exact mechanism of valence reduction is unknown. Dramatic changes in valence state were not observed in the synthetic garnet irradiated in the present study, because Fe^{2+} and Ce^{3+} in the synthetic garnet were already in a reduced state. The change in valence state in an ambient atmosphere, in which the specimens were carried, is negligible because pristine Fe-metal was not oxidized. Also, the thin specimen geometry was not a significant factor in the oxidation of the material. However, some Fe^{3+} in andradite might be reduced to Fe^{2+} during radiation-induced amorphization. As well as the contribution by the ionization effects during the ion irradiation, reduction reactions might be caused by the electron beam during the EELS analysis.

Acknowledgments

The authors thank the staff of the IVEM-Tandem Facility at Argonne National Laboratory for assistance during the ion irradiation experiments. We thank John F. Mansfield, Corinna J. Wauchope, and Kai Sun of the Electron Microbeam Analysis Laboratory at University of Michigan for their support. This work was supported by US DOE, Office of Basic Energy Sciences under grant DE-FGO2-97ER45656.

References

[1] R.C. Ewing, W.J. Weber, F.W. Clinard Jr., Progr. Nucl. Energy 29 (1995) 63.
[2] W.J. Weber, R.C. Ewing, C.R.A. Catlow, T. Diaz de la Rubia, L.W. Hobbs, C. Kinoshita, H.J. Matzke, A.T. Motta, M. Nastasi, E.K.H. Salje, E.R. Vance, S.J. Zinkle, J. Mater. Res. 13 (1998) 1434.
[3] R.C. Ewing, A. Meldrum, L.M. Wang, S.X. Wang, Rev. Min. Geochem. 39 (2000) 319.
[4] R.C. Ewing, W.J. Weber, J. Lian, J. Appl. Phys. 95 (2004) 5949.
[5] B.E. Burakov, E.B. Anderson, D.A. Knecht, M.A. Zamoryanskaya, E.E. Strykanova, M.A. Yagovkina, Mater. Res. Soc. Symp. Proc. 556 (1999) 55.
[6] B.E. Burakov, E.E. Anderson, M.V. Zamoryanskaya, M.A. Petrova, Mater. Res. Soc. Symp. Proc. 608 (2000) 419.
[7] S. Yudintsev, M. Lapina, T. Yudintseva, S. Utsunomiya, L.M. Wang, R.C. Ewing, Mater. Res. Soc. Symp. Proc. 713 (2002) 477.
[8] S. Utsunomiya, L.M. Wang, R.C. Ewing, Nucl. Instrum. and Meth. B 191 (2002) 600.
[9] S. Utsunomiya, L.M. Wang, S. Yudintsev, R.C. Ewing, J. Nucl. Mater. 303 (2002) 177.
[10] S. Utsunomiya, S. Yudintsev, L.M. Wang, R.C. Ewing, J. Nucl. Mater. 322 (2003) 180.
[11] S. Utsunomiya, R.C. Ewing, Environ. Sci. Technol. 37 (2003) 786.
[12] L.M. Wang, R.C. Ewing, MRS Bull. 17 (1992) 38.
[13] J.F. Ziegler, J.P. Birsak, U. Littmark, The Stopping and Range of Ions in Solids, Pergamon, New York, 1985.
[14] R.K. Eby, R.C. Ewing, R.C. Birtcher, J. Mater. Res. 7 (1992) 3080.
[15] S.X. Wang, L.M. Wang, R.C. Ewing, R.H. Doremus, J. Non-Cryst. Solids 238 (1998) 198.
[16] R.E. Williford, R. Devanathan, W.J. Weber, Nucl. Instrum. and Meth. B 141 (1998) 94.
[17] R.F. Egerton, Electron Energy-Loss Spectroscopy in the Electron Microscope, Plenum, New York, 1986.
[18] A. Meldrum, L.A. Boatner, R.C. Ewing, Phys. Rev. B 56 (1997) 13805.
[19] Z.L. Wang, J.M. Cowley, Ultramicroscopy 31 (1989) 437.
[20] S.J. Pennycook, D.E. Jesson, Phys. Rev. Lett. 64 (1990) 938.
[21] S. Utsunomiya, C.S. Palenik, R.C. Ewing, The Dekker Encyclopedia of Nanoscience and Nanotechnology, Marcel Dekker, New York, 2004, p. 1087.
[22] W.J. Weber, Radiat Eff. Def. Solids 115 (1991) 341.
[23] W.J. Weber, R.C. Ewing, L.M. Wang, J. Mater. Res. 9 (1994) 688.
[24] S. Utsunomiya, C.S. Palenik, J.W. Valley, A.J. Cavosie, S.A. Wilde, R.C. Ewing, Geochim. Cosmochim. Acta, in press.
[25] L.A.J. Garvie, P.R. Buseck, J. Phys. Chem. Solids 60 (1999) 1943.
[26] L.A.J. Garvie, P.R. Buseck, Nature 396 (1998) 667.
[27] P.A. van Aken, B. Liebscher, V.J. Styrsa, Phys. Chem. Miner. 25 (1998) 323.
[28] P.A. van Aken, B. Liebscher, Phys. Chem. Miner. 29 (2002) 188.
[29] M. Zang, E.K.H. Salje, R.C. Ewing, J. Phys. Condens. Matter 15 (2003) 3445.